Supporting Information for

An Outer Coordination Sphere Proton Relay Enables Fast Oxidation of H_2 without an Increase in Overpotential with a Bio-Inspired Iron Molecular Electrocatalyst

Jonathan M. Darmon, Neeraj Kumar, Elliott B. Hulley, Charles J. Weiss, Simone Raugei, R. Morris Bullock, and Monte L. Helm*

*To whom correspondence should be addressed.

E-mail: monte.helm@pnnl.gov

Table S1. Selected bond distances (Å) and angles (deg) for **1-Fe*H*(N*H*)**.

Fe(1)–P(1)	2.141(1)
Fe(1)–P(2)	2.1427(9)
Fe(2)–P(3)	2.1580(8)
Fe(2)–P(4)	2.147(1)
P(1)–Fe(1)–P(2)	92.06(3)
Cp^{cent}–Fe(1)–P(1)	130.11
Cp^{cent}–Fe(1)–P(2)	129.22
P(3)–Fe(2)–P(4)	90.10(3)
Cp^{cent}–Fe(2)–P(3)	132.33
Cp^{cent}–Fe(2)–P(4)	128.84

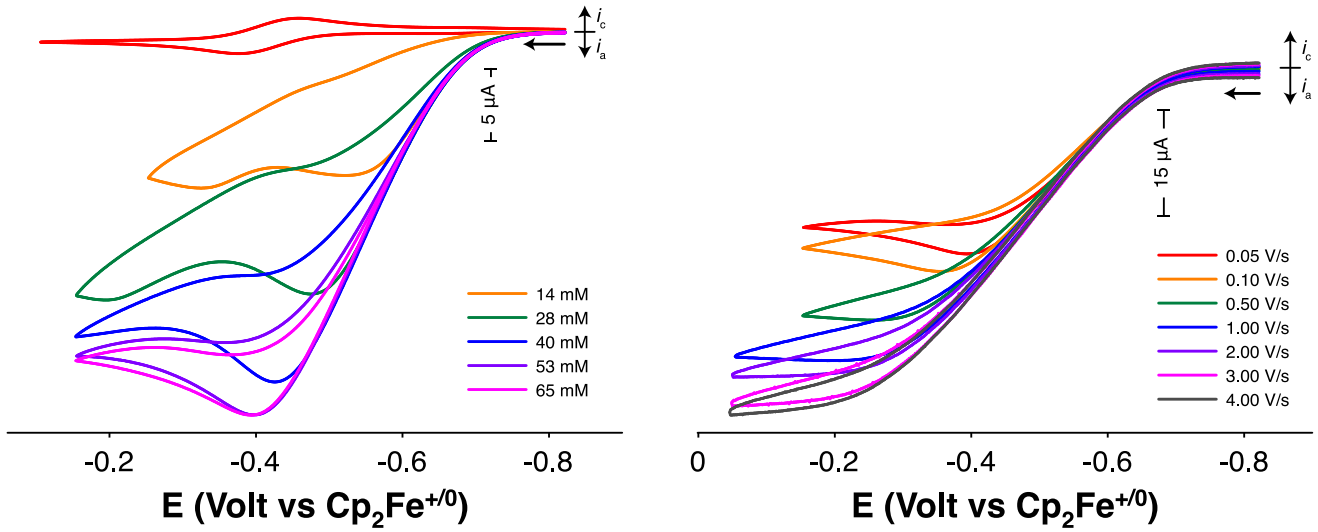

(a) (b)

Figure S1. (a) Cyclic voltammograms of a fluorobenzene solution of **1-Fe*H*(N*H*)** upon addition of *N*-methylpyrrolidine at 50 mV/s. The initial CV (red) corresponds to **1-Cl** prior to activation with $NaBAr^F{}_4$. (b) Cyclic voltammograms of a fluorobenzene solution of **1-H** in the presence of 65 mM *N*-methylpyrrolidine solution as a function of scan rate. Conditions for all experiments: 1 mM [Fe], 0.1 M $[^nBu_4N][B(C_6F_5)_4]$, 1 atm H_2, 22 ºC.

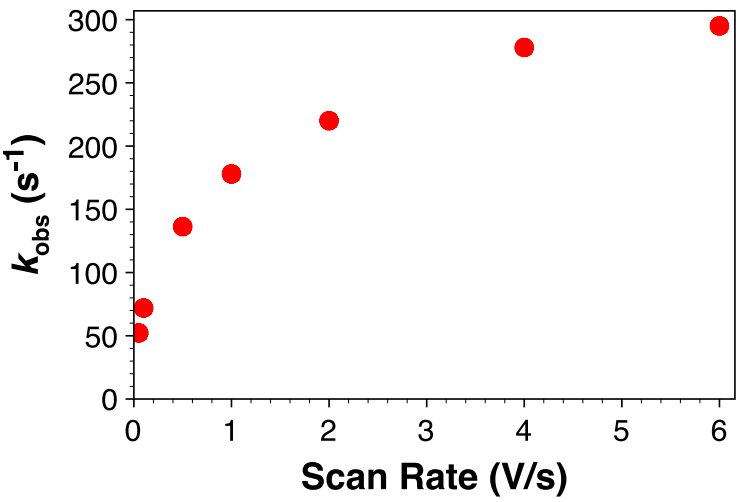

Figure S2. Plot of the turnover frequency (k_{obs}) versus scan rate (V/s) of a fluorobenzene solution of **1-Fe*H*(N*H*)** upon addition of 77 mM DABCO under 1 atm H_2 at 22 ºC. Conditions: 1 mM [Fe], 0.1 M [^{n}Bu$_4$N][B(C$_6$F$_5$)$_4$], 1 atm H_2, 22 ºC.

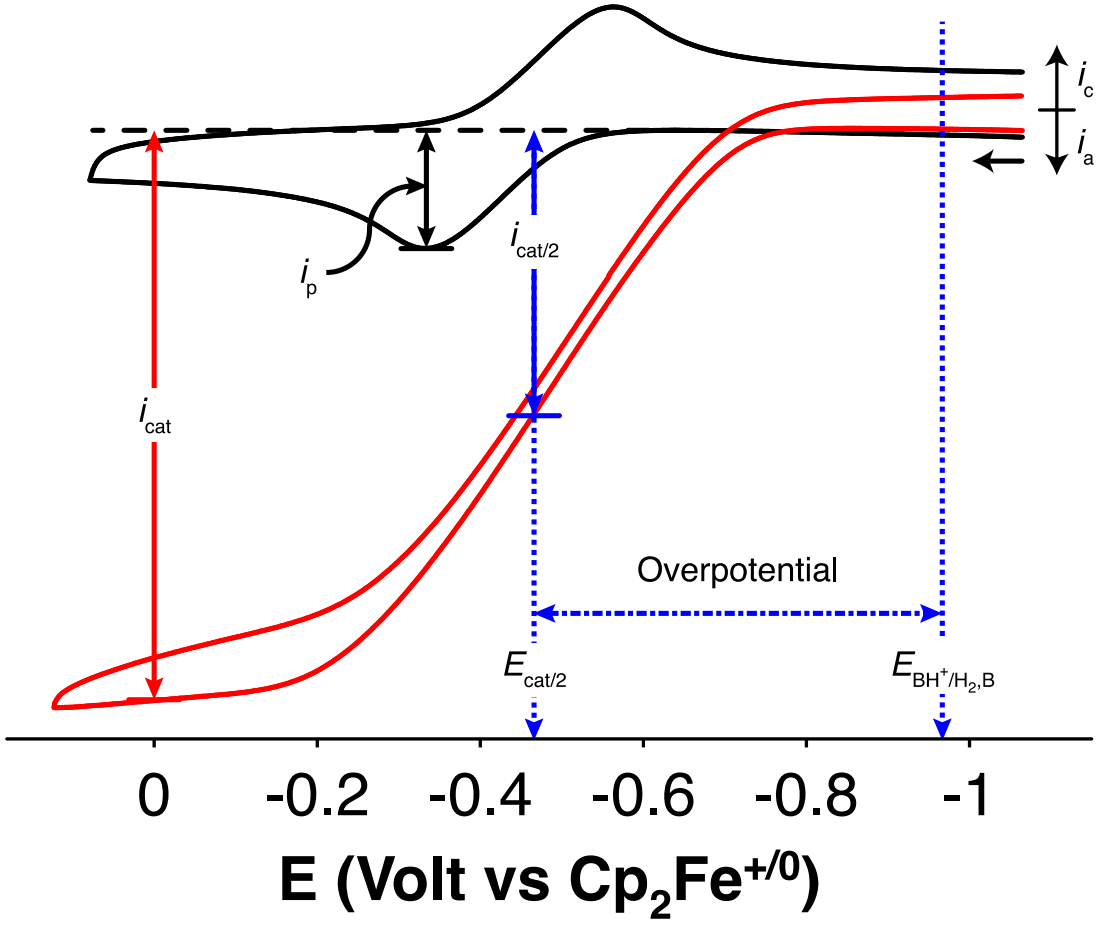

Figure S3. Cyclic voltammograms of a fluorobenzene solution of **1-Cl** (black) and subsequent current enhancement upon addition of $NaBAr^F{}_4$, 1 atm H_2, and 77 mM DABCO (red). Conditions: 1 mM [Fe], 0.1 M [^{n}Bu$_4$N][B(C_6F_5)$_4$], 1 atm H_2, 6 V/s.

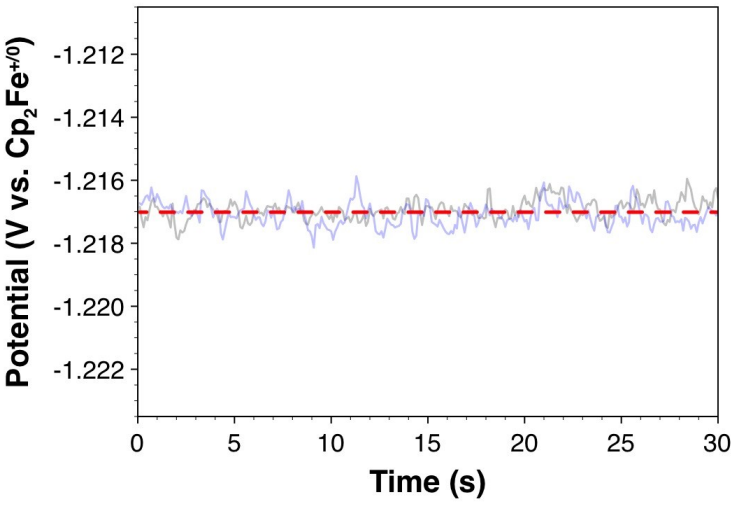

(a)

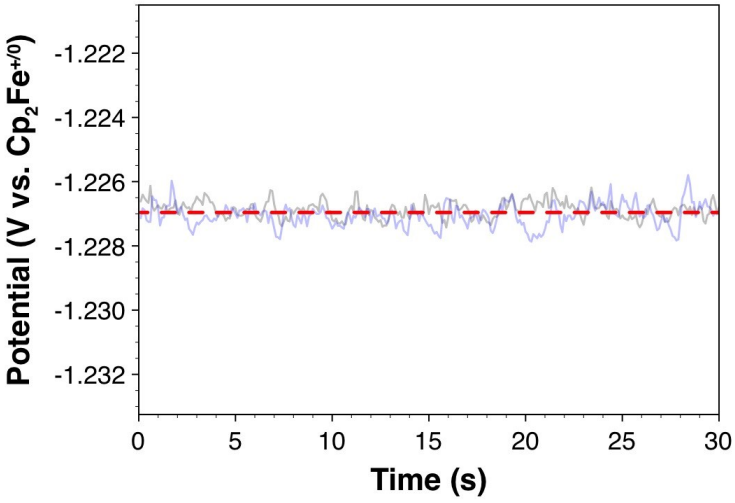

(b)

Figure S4. Open circuit potential of a platinum electrode vs. $Fc^{+/0}$ as a function of time, used to determine E_{BH+} under buffered conditions (10:1 DABCO to DABCO-H^+). Two consecutive measurements, shown in black and blue are presented to demonstrate the stability of the open circuit potential. Conditions: 89 mM DABCO, 9.9 mM $[(DABCO)_2H][B(C_6F_5)_4]$, 0.1 M $[Bu_4N][B(C_6F_5)_4]$, fluorobenzene solution, 22 ºC, 1 atm H_2.

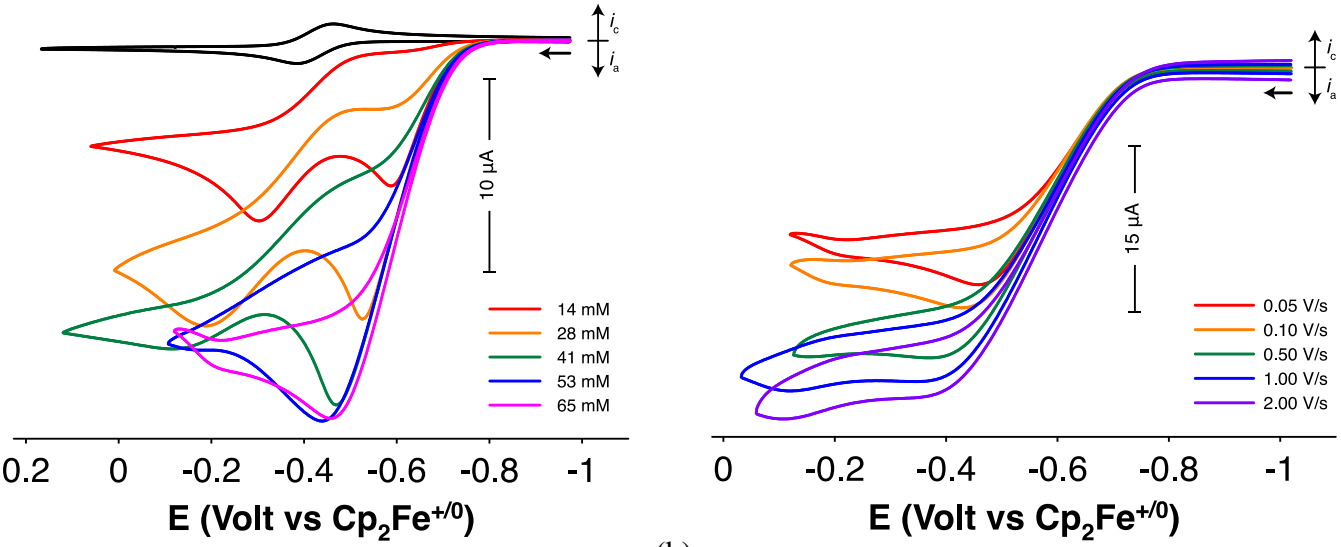

(a) (b)

Figure S5. (a) Cyclic voltammograms of a fluorobenzene solution of **1-Fe*H*(N*H*)** upon addition of buffered DABCO at 50 mV/s. The initial CV (black) corresponds to **1-Cl** prior to activation with $NaBAr^F{}_4$. (b) Cyclic voltammograms of a fluorobenzene solution of **1-H** in the presence of 65 mM buffered DABCO as a function of scan rate. Conditions for all experiments: 1 mM [Fe], 0.1 M [^{n}Bu$_4$N][B(C$_6$F$_5$)$_4$], 1 atm H_2, 22 ºC.

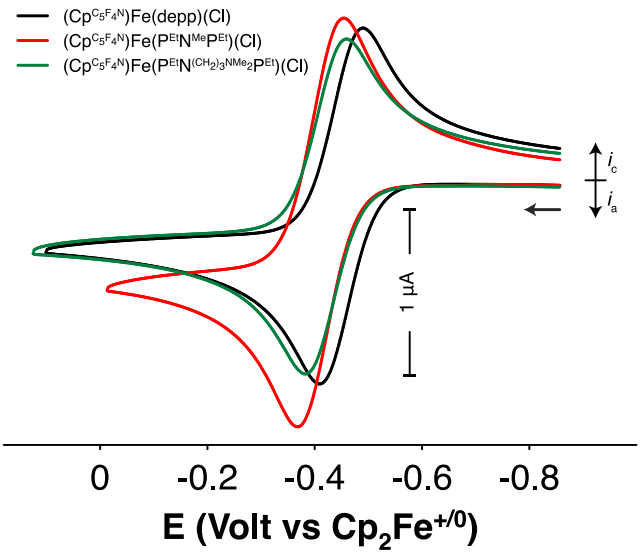

Figure S6. Overlay of cyclic voltammograms of (Cp^{C5F4N})Fe(depp)(Cl), (Cp^{C5F4N})Fe($P^{Et}N^{Me}P^{Et}$)(Cl), and (Cp^{C5F4N})Fe($P^{Et}N^{(CH2)3NMe2}P^{Et}$)(Cl) (**1-Cl**) in fluorobenzene at 50 mV/s. Conditions: 1 mM [Fe], 0.1 M [$^{n}Bu_4N$][$B(C_6F_5)_4$], 22 ºC.

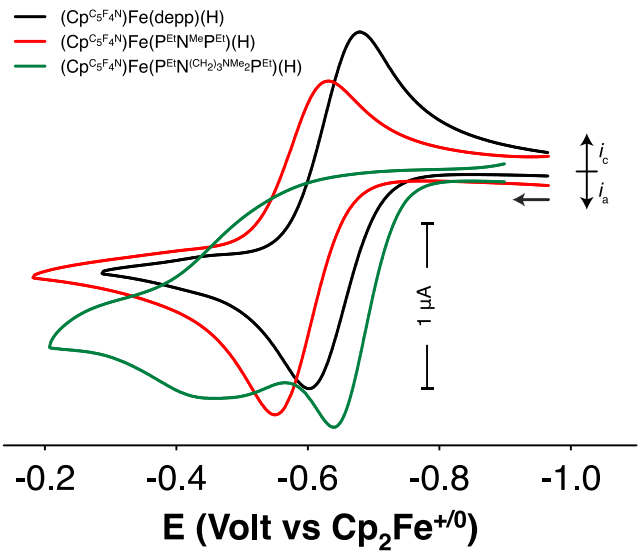

Figure S7. Overlay of cyclic voltammograms of (Cp^{C5F4N})Fe(depp)(H), (Cp^{C5F4N})Fe($P^{Et}N^{Me}P^{Et}$)(H), and (Cp^{C5F4N})Fe($P^{Et}N^{(CH2)3NMe2}P^{Et}$)(H) (**1-H**) in fluorobenzene at 50 mV/s. Conditions: 1 mM [Fe], 0.1 M [$^{n}Bu_4N$][$B(C_6F_5)_4$], 22 ºC.

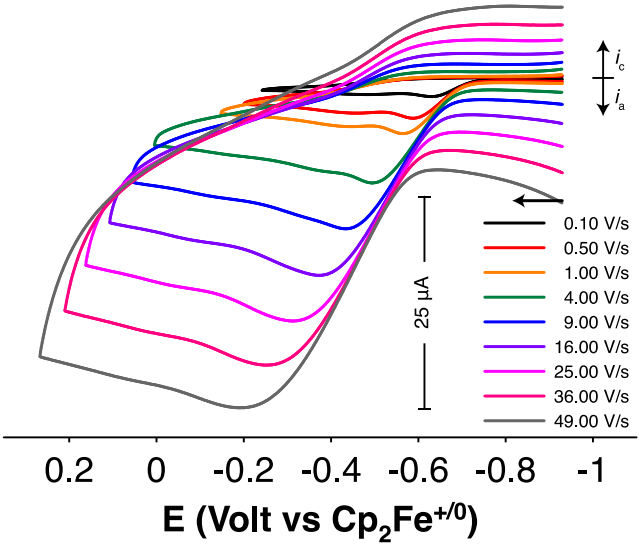

Figure S8. Cyclic voltammograms of a fluorobenzene solution of (Cp^{C5F4N})Fe($P^{Et}N^{(CH2)3NMe2}P^{Et}$)(H) (**1-H**) at scan rates between 0.05–50 V/s. Conditions: 1 mM [Fe], 0.1 M [$^{n}Bu_4N$][$B(C_6F_5)_4$], 22 ºC.

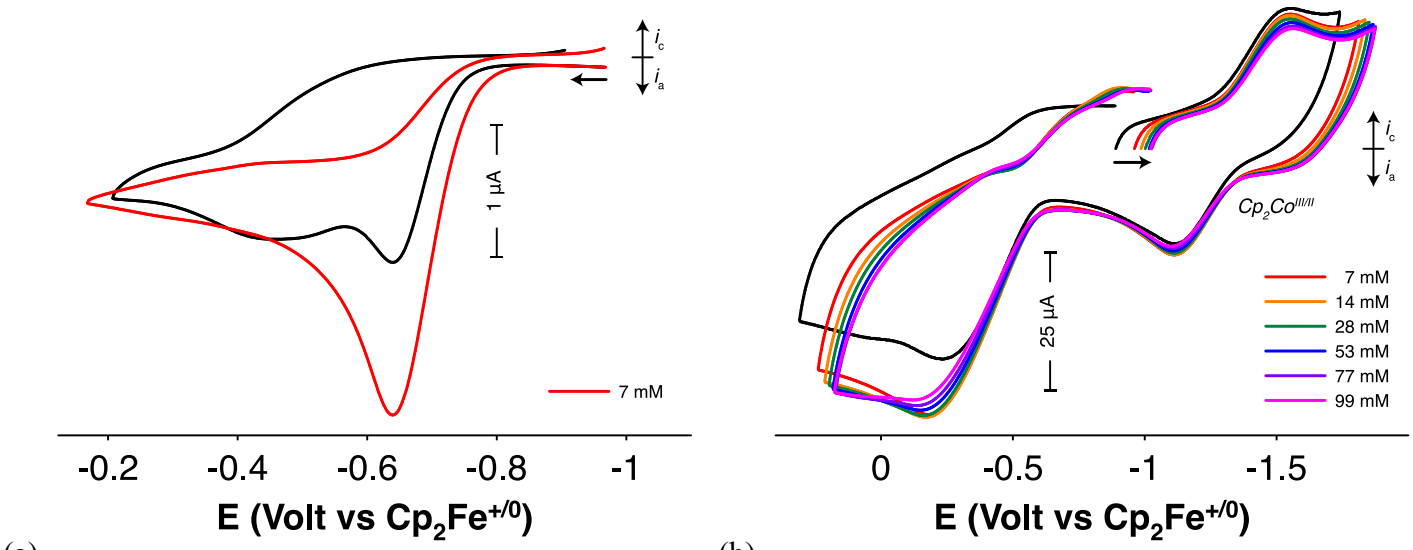

(a) (b)

Figure S9. (a) Cyclic voltammograms of a fluorobenzene solution of (Cp^{C5F4N})Fe($P^{Et}N^{(CH2)3NMe2}P^{Et}$)(H) (**1-H**) in the presence of *N*-methylpyrrolidine at 50 mV/s. (b) Cyclic voltammograms of a fluorobenzene solution of (Cp^{C5F4N})Fe($P^{Et}N^{(CH2)3NMe2}P^{Et}$)(H) (**1-H**) in the presence of *N*-methylpyrrolidine at 50 V/s. In both figures, the initial CV (black) corresponds to **1-H** prior to addition of exogenous base. Conditions for all experiments: 1 mM [Fe], 0.1 M [^{n}Bu$_4$N][B(C$_6$F$_5$)$_4$], 22 ºC.

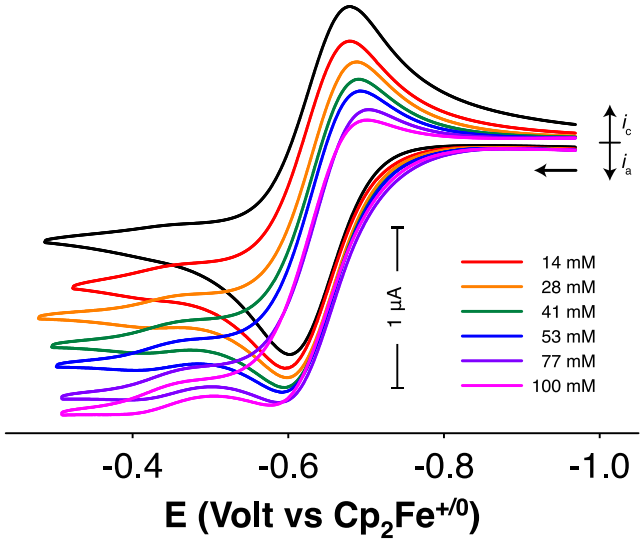

Figure S10. Cyclic voltammograms of a fluorobenzene solution of $(Cp^{C5F4N})Fe(depp)(H)$ upon addition of DABCO at 50 mV/s. The initial CV (black) corresponds to $(Cp^{C5F4N})Fe(depp)(H)$ in the absence of DABCO. Conditions: 1 mM [Fe], 0.1 M $[^nBu_4N][B(C_6F_5)_4]$, 1 atm H_2, 22 ºC.

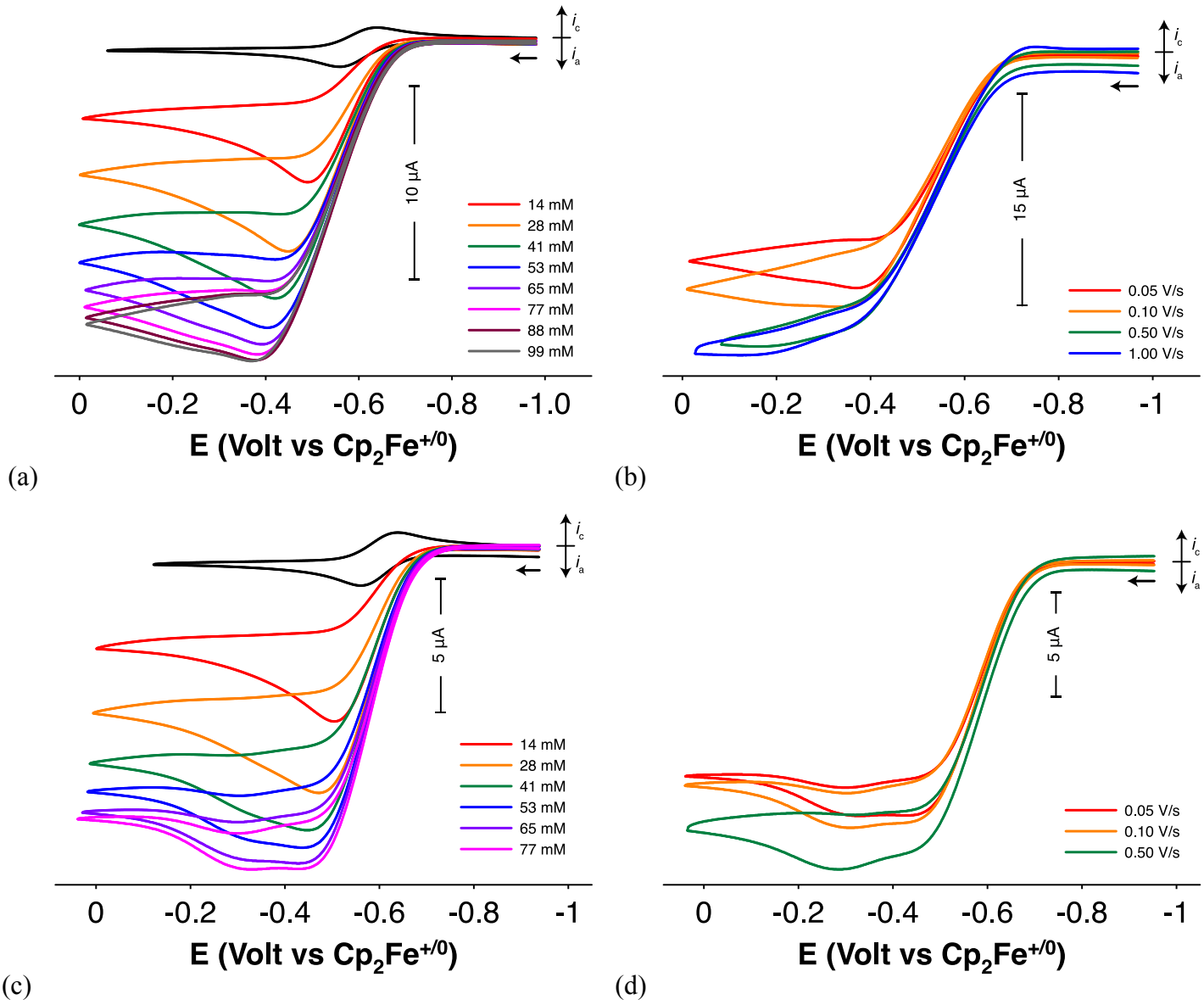

Figure S11. (a) Cyclic voltammograms of a fluorobenzene solution of $(Cp^{C5F4N})Fe(P^{Et}N^{Me}P^{Et})(H)$ upon addition of DABCO at 50 mV/s. (b) Cyclic voltammograms of a fluorobenzene solution of $(Cp^{C5F4N})Fe(P^{Et}N^{Me}P^{Et})(H)$ in the presence of 0.1 M DABCO as a function of scan rate. (c) Cyclic voltammograms of a fluorobenzene solution of $(Cp^{C5F4N})Fe(P^{Et}N^{Me}P^{Et})(H)$ upon addition of buffered DABCO at 50 mV/s. (d) Cyclic voltammograms of a fluorobenzene solution of **1-H** in the presence of 77 mM buffered DABCO as a function of scan rate.

In (a) and (c), the initial CV (black) corresponds to $(Cp^{C5F4N})Fe(P^{Et}N^{Me}P^{Et})(H)$ prior to addition of exogenous base. Conditions for all experiments: 1 mM [Fe], 0.1 M $[^{n}Bu_4N][B(C_6F_5)_4]$, 1 atm H_2, 22 ºC.

Computational Analysis of the Catalytic Mechanism

Previous computational and experimental investigations of the $[(Cp^{C5F4N})Fe(P^{R}N^{R'}P^{R})]^{+}$ family of compounds indicated that the intramolecular followed by intermolecular deprotonation steps of the Fe(III) hydride (*e.g.*, steps 6-8, Fig. S7) are the turnover limiting steps in the overall observed rate of catalysis. Additional calculations suggest that the free energy barrier for these deprotonation events is very similar (17.1 and 17.6 kcal/mol, respectively, see Fig. S9, grey trace), indicating that both steps equally influence the overall catalytic rate of the $P^{Et}N^{Me}P^{Et}$ family. Lowering the barrier for intermolecular deprotonation and making intramolecular deprotonation thermodynamically more favorable for the Fe(III) hydride was the main motivation for appending an additional proton relay in the outer coordination sphere. The detailed computational analysis reported below shows that addition of an outer coordination sphere pendant amine makes the intramolecular proton transfer from the metal center to the second coordination sphere amine more favorable, and results from a 2.7 pK_a unit increase in the basicity of the second coordination sphere amine as compared to $[(Cp^{C5F4N})Fe(P^{Et}N^{Me}P^{Et})]^{+}$ (Fig. S9). In addition, the activation free energy for this intramolecular deprotonation is reduced by 2 kcal/mol (step 6, Fig. S9) compared to the same barrier in the complex without an outer sphere pendant amine (Fig. S9).

The proposed catalytic cycle for H_2 oxidation by $[(Cp^{C5F4N})Fe(P^{Et}N^{(CH2)3NMe2}P^{Et})]^{+}$ is shown in Fig. S7 and consists of alternating electron transfer and intra- and intermolecular proton transfer steps. Detailed information for all of the possible catalytic intermediates as well as transition states for each step is presented in Fig. S8 and S9. Addition of H_2 to the 16-electron Fe(II) complex leads to the formation of an $Fe(\eta^2\text{-}H_2)^{+}$ adduct (**RC**, Fig. S8) with a ΔG of –8.5 kcal/mol. The dihydrogen adduct undergoes an easy chair-to-boat isomerization of the six-membered ring identified by the phosphine ligand and the metal center, populating the intermediate species **Int1** (Fig. S8). The presence of the pendant amine facilitates the heterolytic cleavage of H_2 (**TS2**, Fig. S8, $\Delta G^{\ddagger}$ = 7.5 kcal/mol) with the formation of a N-protonated Fe(II) hydride species **Int2** (Fig. S8).

The protonated pendant amine in **Int2** is stabilized by intramolecular hydrogen with the outer coordination sphere pendant amine. The protic hydrogen is promptly transferred between the two amine functions, yielding the intermediate **Int3-p**, which easily opens the six membered ring, exposing the protonated secondary amine to the exogenous base in solution (Fig. S8). The proton hydride species **Int3-p** is almost isoenergetic with the Fe(η^2-H_2) adduct. This finding, along with the relatively small activation barrier for the H_2 splitting and subsequent proton reorganization, suggests that in the absence of a deprotonating agent these two species are in rapid, dynamic equilibrium. Variable temperature NMR studies confirmed fast proton and hydride exchange. The first deprotonation of **Int3-p** by *N*-methylpyrrolidine is fast ($\Delta G^{\ddagger}$ = 2.6 kcal/mol) with a ΔG of –3.2 kcal/mol (step 4, Fig. S7). The computed kinetic and thermodynamic parameters of the initial catalytic steps suggest that all of these steps (Fig. S8) are suitably energy matched with free energy barriers under 9 kcal/mol), and therefore do not contribute to the rate limiting step.

The pK_a value of the Fe(II) hydride is too large compared to the second coordination sphere pendant amine, which prevents intramolecular proton transfer. Oxidation to the resulting Fe(III) hydride reduces its pK_a value, allowing for more facile intra- and intermolecular proton transfers. The free energy profile for various possible deprotonation routes of the Fe(III) hydride is shown in Fig. S9. The lowest free energy pathway consists of a step-wise proton movement (Fig. S9, red trace) from the metal center to the second- and then the outer coordination sphere amine, followed by intermolecular deprotonation by the exogenous base (Fig. S7, steps 6, 7 and 8). The largest barrier for the second deprotonation is the initial proton movement from the Fe(III) hydride to the second coordination sphere amine ($\mathbf{\Delta} G^{\ddagger}$ = 15.1 kcal/mol). This is the catalytic rate-limiting step (step 6, Fig. S7). The magnitude of the barrier for this deprotonation is a consequence of the significant difference in acidity between the Fe(III) hydride and the protonated pendant amine (6.2 pK_a units), which makes the intramolecular proton transfer endothermic by $\mathbf{\Delta} G^{\mathbf{intra}}$ = 8.5 kcal/mol. It is important to point out that the presence of the outer coordination sphere amine stabilizes the protonated amine in the second coordination

sphere intermediate via intramolecular hydrogen bonding, which results in a decrease of the pK_a difference between the Fe(III) hydride intermediate and protonated amine relative to the $[(Cp^{C5F4N})Fe(P^{Et}N^{Me}P^{Et})]^+$ complex by more than 2.7 pK_a units. Similarly, the intramolecular deprotonation of the Fe(III) hydride has an activation free energy of about 2 kcal/mol lower than in the $P^{Et}N^{Me}P^{Et}$ complex (Fig. S9, grey trace). The intramolecular proton transfer between the secondary and outer pendant amines is very facile in contrast to the direct deprotonation from the second coordination sphere ammonium in $[(Cp^{C5F4N})Fe(P^{Et}N^{Me}P^{Et})]^+$ (Fig. S9, grey trace). The intramolecular hydrogen bond between the two pendant amines is easily broken, exposing the protonated outer sphere amine to the exogenous base, which deprotonates it with a free energy barrier relative to the Fe(III) hydride of only 8.6 kcal/mol.

Alternative deprotonation pathways were also considered and explored computationally. Direct intermolecular deprotonation from either the Fe(III) hydride (Fig. S9, step 6a) or the second coordination sphere ammonium (Fig. S9, step 7a) has a considerably higher free energy barrier ($\Delta G^{\ddagger,inter}$ = 31.7 kcal/mol and 20.2 kcal/mol, respectively). The origin of the kinetic penalty for these two alternative deprotonation pathways is related the steric accessibility as discussed in our earlier work. Intramoleclar deprotonation of the Fe(III) hydride by the outer coordination sphere amine also presents an appreciably high activation barrier ($\Delta G^{\ddagger,\ intera}$ = 25.7 kcal/mol), again due to the steric accessibility to the hydride position.

The present calculations clearly show that the introduction of an additional proton relay in the outer coordination sphere of the catalyst creates a suitable pathway for the proton movement from the metal center to the periphery of the catalysts, resulting from the increased basicity of the second coordination sphere and the elimination of any steric penalty for the final deprotonation by the exogenous base.

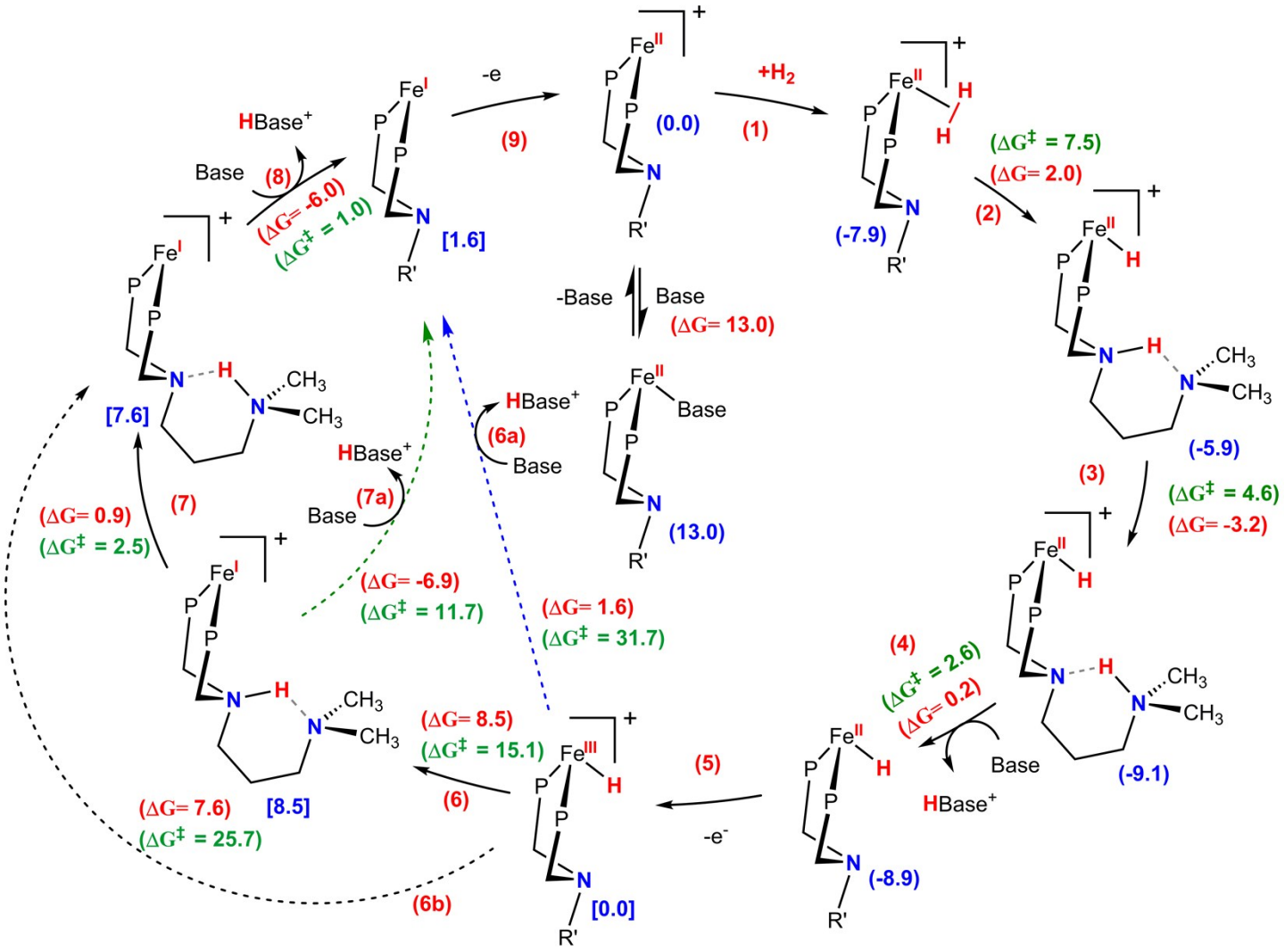

Figure S12. Proposed mechanism for the electrocatalytic oxidation of H_2 by $[(Cp^{C5F4N})Fe(P^{Et}N^{(CH2)3NMe2}P^{Et})]^+$ using *N*-methylpyrrolidine as the exogenous base where reaction free energy (ΔG) of each step is shown in red, free energy barriers ($\Delta G^{\ddagger}$) are shown in green. The free energy of the reaction, shown in blue, is relative to the isolated Fe^{II} cationic species, and the one in square brackets is relative to the Fe^{III}-H cationic species.

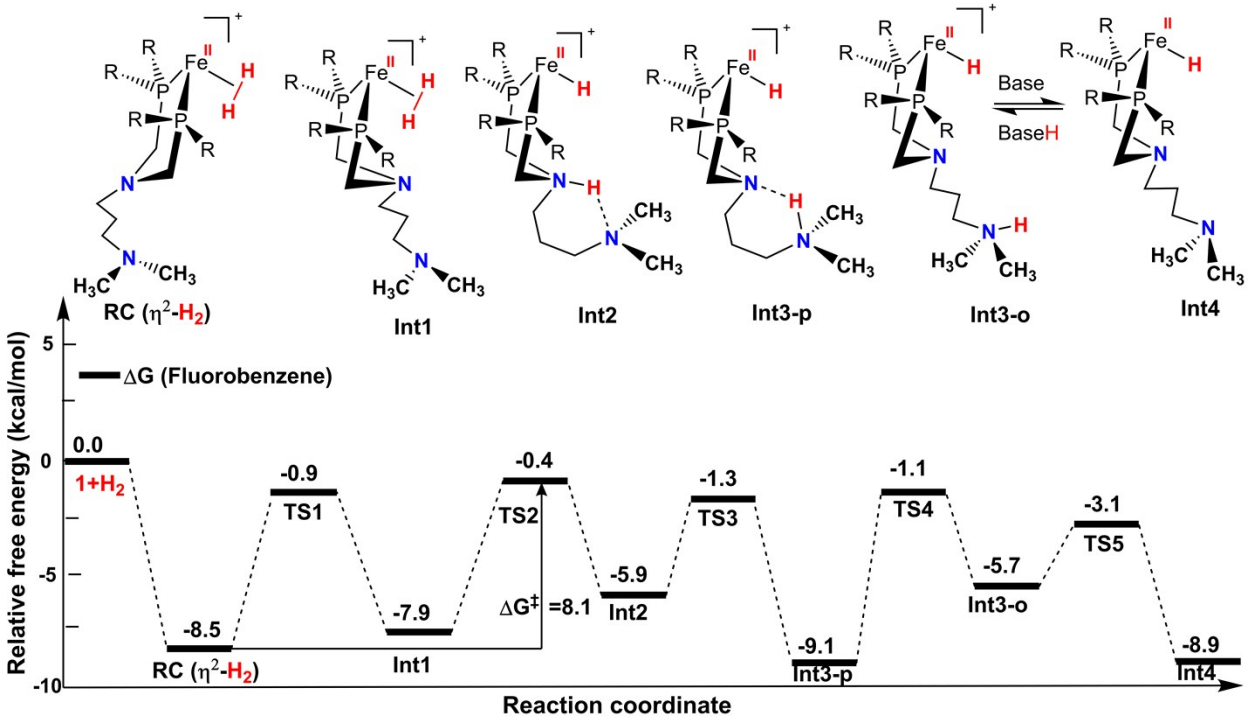

Figure. S13. Free energy profile of initial catalytic steps for the oxidation of H_2 by $[(Cp^{C5F4N})Fe(P^{Et}N^{(CH2)3NMe2}P^{Et})]^+$.

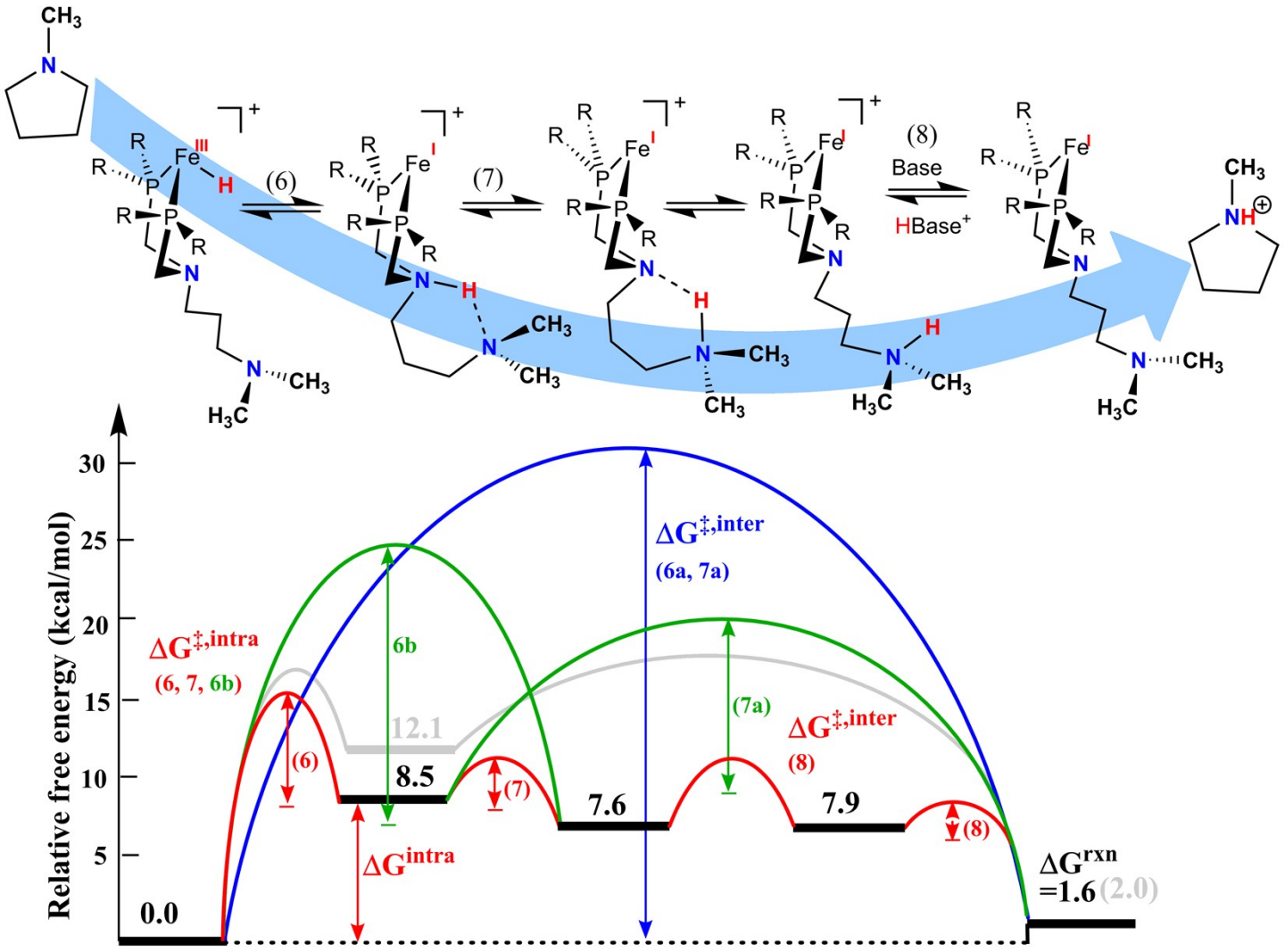

Figure S14. Free energy diagram for the intra- and intermolecular deprotonation of $[(Cp^{C5F4N})Fe(P^{Et}N^{(CH2)3NMe2}P^{Et})H]^+$ by *N*-methylpyrrolidine computed using DFT calculations. All reaction free energies and barriers are presented as solid lines. The solid red lines represent deprotonation of the Fe(III) hydride by second and outer sphere pendant amines and subsequent deprotonation by the exogenous base, indicating the minimum energy pathway for proton movements (steps 6, 7 and 8, Figure S1) away from the Fe(III) active site, *i.e.*, a proton channel pathway. The blue line represents direct deprotonation of the Fe(III) hydride by the exogenous base (step 6a, Figure S1). The green line represents direct deprotonation of the Fe(III) hydride by outer sphere pendant amine (step 6b, Figure S1) and deprotonation of the second sphere pendant amine by the exogenous base (step 7a, Figure S1). The solid grey line represents the intra- followed by intermolecular deprotonation by the exogenous base of the Fe(III) hydride for $P^{Et}N^{Me}P^{Et}$ $[(Cp^{C5F4N})Fe(P^{Et}N^{Me}P^{Et})]^+$, i.e., without the outer sphere pendant amine.

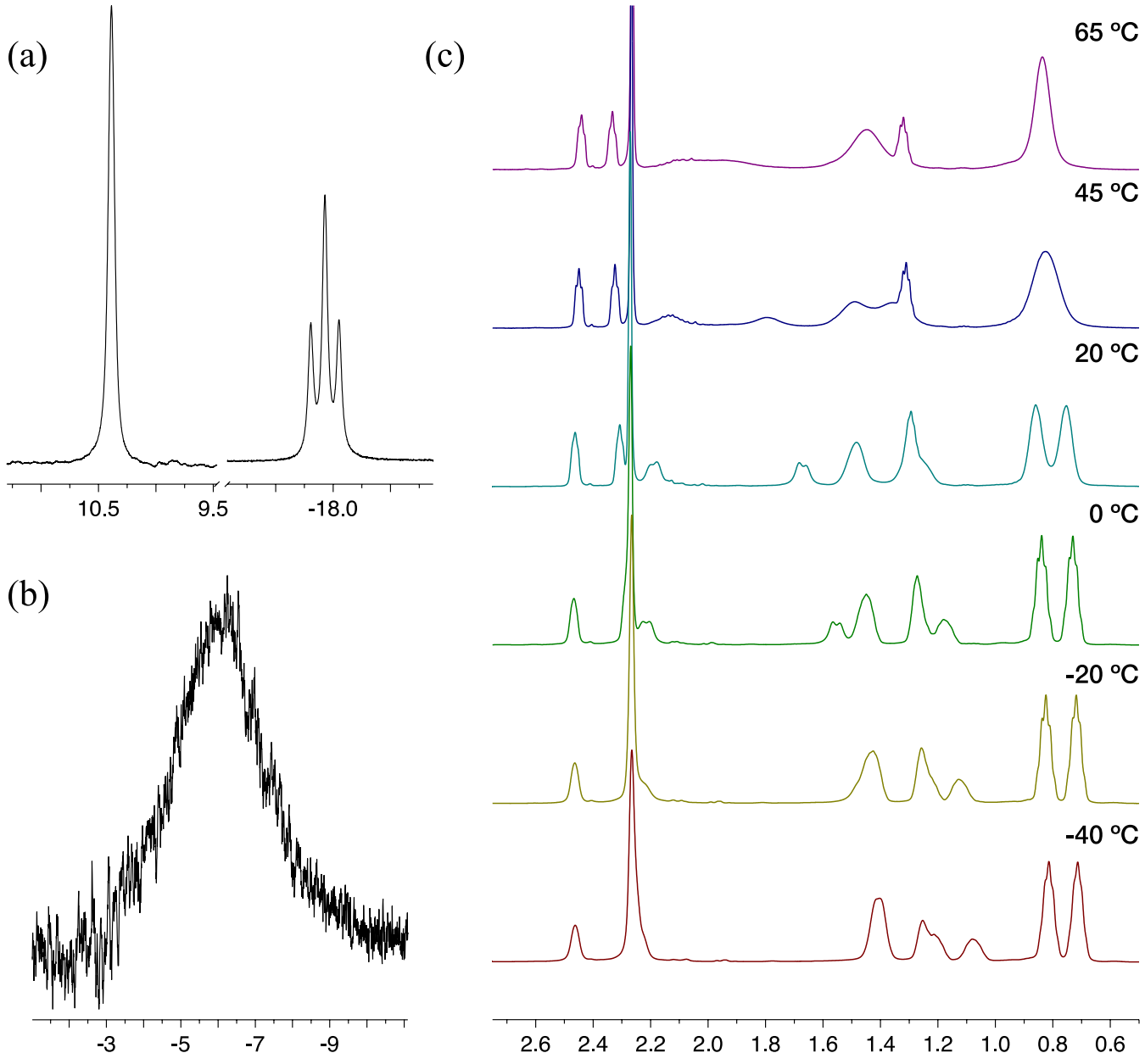

Fig. S15. Selected regions of ^{1}H NMR spectra of a fluorobenzene solution of **1-Fe*H*(N*H*)** under 1 atm of H_2 between -40 and 65 ºC. (a) ^{1}H NMR resonances corresponding to the proton (left, 10.4 ppm) and hydride (right, -17.9 ppm, J_{PH} = 62 Hz) observed at -40 ºC. (b) ^{1}H NMR spectrum of the coalesced proton and hydride resonances (-6.1 ppm) observed at 65 ºC. (c) Dynamic ^{1}H NMR behavior observed from 0 and 3 ppm between -40 and 65 ºC.

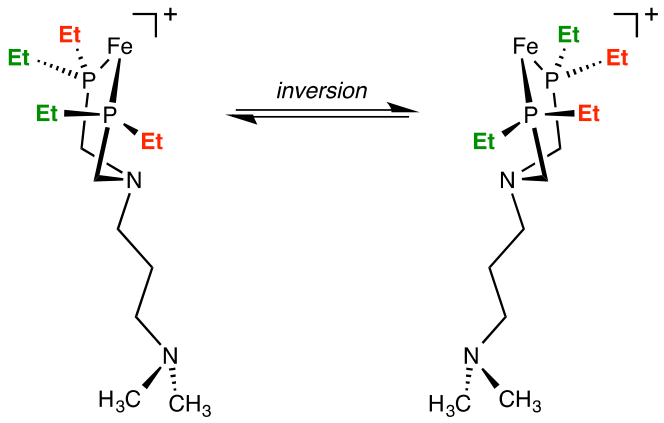

Figure S16. Iron-PNP inversion behavior observed by ^{1}H NMR spectroscopy during variable temperature studies of **1-Fe*H*(N*H*)**.

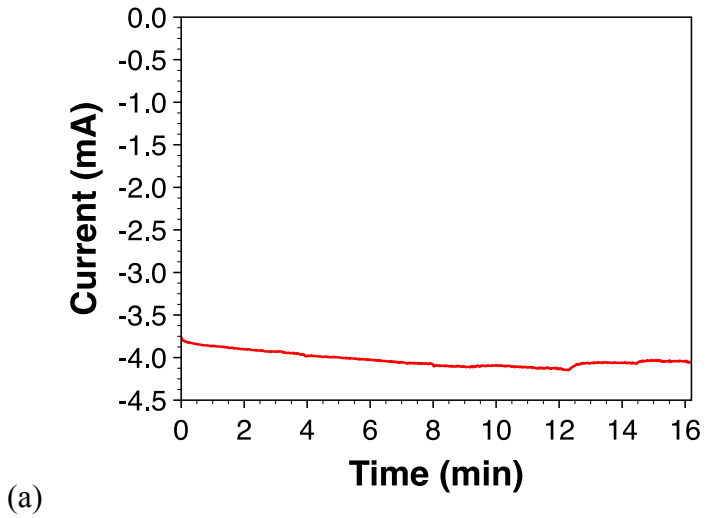

(a)

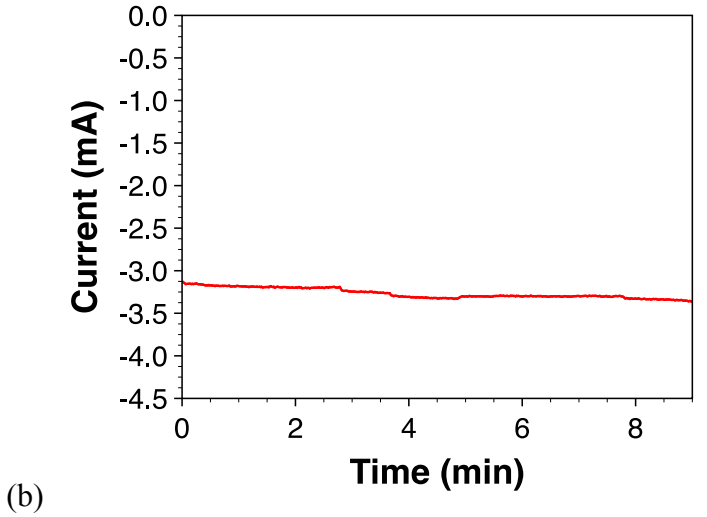

(b)

Figure S17. Plot of current versus time after passing (a) 4.01 C, and (b) an additional 1.89 C (5.90 C total) during the bulk electrolysis experiment.

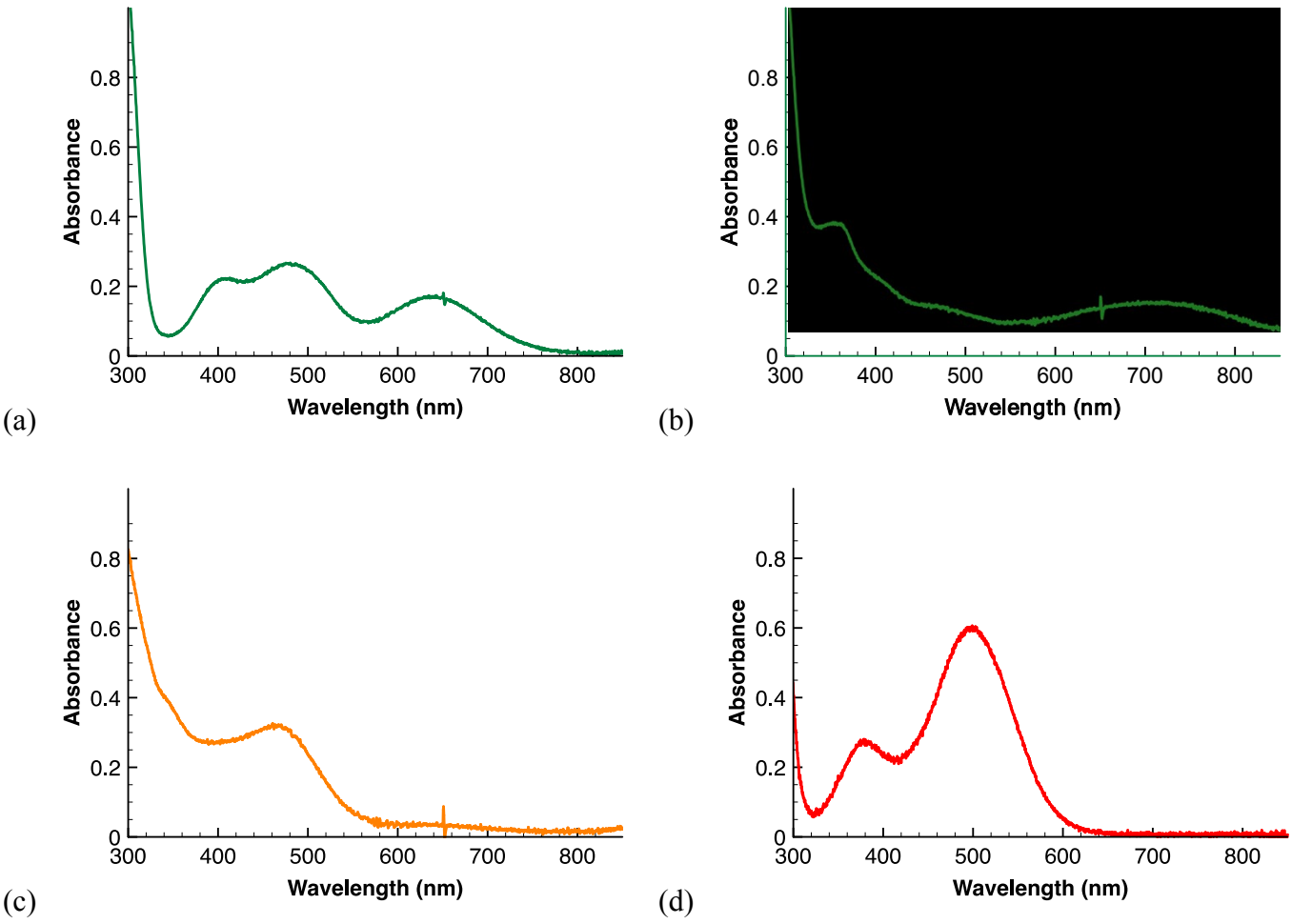

Fig. S18. UV-Vis spectra of (a) **1-Cl** (green), (b) [(Cp^{C5F4N})Fe($P^{Et}N^{(CH2)3NMe2}P^{Et}$)][$BAr^{F}_{4}$] (light green) (c) **1-Fe*H*(N*H*)** (orange) and (d) **1-H** (red). All solutions were ~0.1 mM [Fe] in fluorobenzene at 22 ºC. Spectrum (b) was prepared by treating the stock solution of (Cp^{C5F4N})Fe($P^{Et}N^{(CH2)NMe2}P^{Et}$)(Cl) with excess $NaBAr^{F}_{4}$ and stirring for 15 minutes, and (c) was collected after bubbling hydrogen into the solution for 30 seconds.